EVS29 Symposium
Montréal, Québec, Canada, June 19-22, 2016

Driving-Scenario Oriented Optimal Design of an Axial-Flux Permanent-Magnet Motor for an Electric Vehicle

Guan-Yu Shih[1] and Yee-Pien Yang[1,2]

[1]*Department of Mechanical Engineering, National Taiwan University, Taipei, Taiwan 10617*

[2]*Industrial Technology Research Institute, Hsinchu, Taiwan 31040*

[1]*ypyang@ntu.edu.tw;* [2]*yeeyang@itri.org.tw*

Summary

This paper proposes a driving-scenario oriented optimal design of an axial-flux permanent-magnet (AFPM) motor for an electric vehicle. The target torque and speed (TN) curve is defined as three operation zones—constant torque, maximum direct current, and maximum voltage—based on the driving scenario. The AFPM motor is designed to minimize energy consumption based on the motor weight and the frequent operating points of a driving cycle. The final result shows that the electric vehicle driven by the proposed AFPM motor consumes about 15% less energy than motors designed using traditional methods.

Keywords: electric vehicle, permanent magnet motor, brushless motor, motor design, optimization

1 Introduction

Increasing concerns about the natural environment and growing shortages of petroleum resources have driven many researchers to develop electric vehicles (EV). Due to a wide range of variable driving circumstances, such as load and vehicle speed, the operating point of a motor constantly changes. The working area of the motor, which matches a driving scenario involving accelerating, cruising, and slope climbing, is the main requirement for motor design.

EV motors are traditionally designed to satisfy the basic requirements of rated or maximum power, torque, and speed based on the driving conditions of acceleration and speed. For example, Kahourzade et al. [1] discussed a comprehensive design of a 10-kW AFPM motor for an EV direct drive based on the power and torque requirement. Lindh et al. [2] designed an interior permanent-magnet synchronous motor (PMSM) for traction application to meet the requirements of torque and speed under the constraints of voltage and current using an optimization process; however, the resulting torque and speed (TN) curve was determined by tuning the number of turns, the torque, and the current ratio. One drawback of the traditional motor design is that a close relationship does not exist between the TN curve and the motor parameters. Recently, the integration of driving cycles into the design optimization of an electric driveline has received limited attention in the literature.

This paper proposes a novel approach for designing an AFPM motor for EVs. The design methodology is divided into four stages. First, a target TN curve based on a driving scenario, battery capabilities, motor drive pattern, and basic torque and voltage equations of the proposed motor is specified in Section 2. This target TN curve is closely related to the back electromotive force (EMF) constant, phase inductance, and phase resistance of the motor. Second, the magnetic circuit model with a quasi-3-dimensional (quasi-3D) motor configuration is provided in Section 3. Third, an optimal motor shape is determined using three

objectives—minimizing motor weight, maximizing motor efficiency at the rated operating point, and minimizing energy loss over various driving cycles—as described in Section 4. Fourth, FE verification of the proposed motor is presented in Section 5. Finally, Section 6 presents the study's conclusions.

2 Specifications and Target TN Curve

The proposed traction motor is designed for a four-wheel-drive passenger car weighing 1800 kg. Each wheel radius of 0.317 m is driven by an AFPM motor with a planetary reduction gear of ratio 4:1, as shown in Fig. 1. A novel design methodology is proposed based on the driving scenario and the motor's torque, speed, and power performance boundaries. The motor's target TN curve is then determined using battery specifications and motor drive properties.

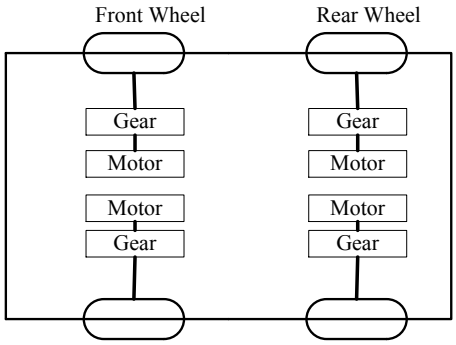

Figure 1: A schematic view of a four-wheel-drive electric passenger car

2.1 Driving Scenario

Based on the vehicle data and performance requirements related to acceleration and hill-climbing ability, torque for one motor sharing 25% of the traction force T and motor speed ω is expressed as

$$T = \frac{r}{4\eta\kappa}\left(\gamma\, ma + \frac{\rho}{2} C_D A_f V_r^2 + f_r mg\cos\theta + mg\sin\theta\right) \tag{1}$$

$$\omega = \frac{v}{r\left(1 - \lambda_w\right)} \tag{2}$$

where r is the wheel radius, η is the mechanical efficiency, κ is the gear ratio, γ is the equivalent mass coefficient, m is the vehicle mass, a is the acceleration, ρ is the air mass density, C_D is the aerodynamic coefficient, A_f is the frontal area of the vehicle, V_r is the relative velocity between the air and the vehicle, f_r is the rolling resistance factor, g is the gravitational constant, θ is the slope angle, v is the vehicle speed, and λ_w is the slip between the wheel and the road. Detailed vehicle parameters are provided in Table 1.

Table 1: Vehicle parameters and motor specifications

Parameter (Unit)	Value
Radius of wheels (m)	0.317
Vehicle mass (kg)	1800
Equivalent mass coefficient	1.08
Gravitational acceleration (m/s^2)	9.81
Rolling resistance factor	0.013
Air mass density (kg/m^3)	1.225
Aerodynamic coefficient	0.28
Frontal area of the vehicle (m^2)	1.6
Gear ratio	4:1
Maximum DC voltage (V)	380
Maximum motor output power (kW)	20.4

Three driving scenarios were determined before the motor was designed: (1) the maximum slope that the vehicle can ride at a low speed is 35%; (2) the vehicle can provide maximum acceleration under 40 km/hr; and (3) the maximum cruise speed on a road with a 5% slope is 120 km/hr. The torque production required by the motor was obtained as a function of the vehicle speed and the road slope, which are shown as dotted

lines on the TN coordinates presented in Fig. 2. The required maximum motor torque is about 133.2 Nm at point A for the vehicle riding on a road with a maximum slope of 35% at a very low speed. The maximum output power, P_m=20.4 kW, of the motor is then required in order for the vehicle to reach the speed of 40 km/hr at point B. According to the thermal constraint, the continuous motor torque is set as half of the maximum torque. The continuous motor power, P_c=13.4 kW, is a hyperbolic curve, while the maximum motor speed occurs at point C for the vehicle cruising at its maximum speed of 120 km/hr on a 5% slope (approximate motor speed ω_c=4094 rpm). Here, the maximum and continuous TN curves set the performance requirement of a motor for an EV.

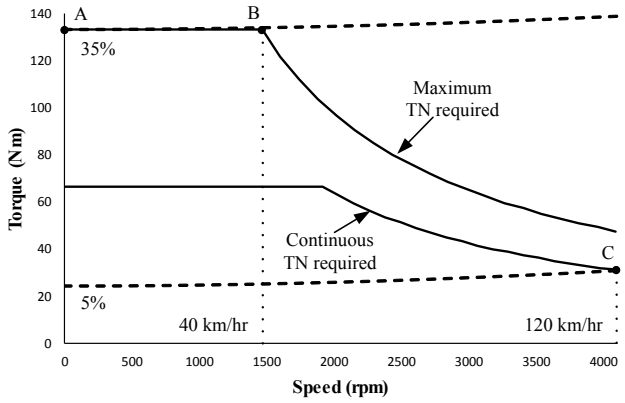

Figure 2: TN curve requirement for one motor

2.2 Motor Equations

The two-axis voltage equations of a PM motor are usually expressed as

$$V_d = R_{ph} i_d - L_q i_q N_p \omega \tag{3}$$

$$V_q = R_{ph} i_q + L_d i_d N_p \omega + K_e \omega \tag{4}$$

where V_d, V_q, i_d, i_q, L_d, and L_q are the d-q-axis voltages, currents, and inductance, respectively; K_e is the back EMF constant of the motor; R_{ph} is the phase resistance; ω is the mechanical speed of the motor; and N_p is the number of pole pairs.

Because this motor has surface-mounted PMs, L_d and L_q can be assumed to be equal to the phase inductance L_{ph}. When the peak of the sinusoidal phase current of the motor I_{ph} is fed on the q-axis, i_d=0 and i_q=I_{ph}. The torque equation is simply expressed as

$$T = \frac{3K_e V_{ph}}{2R_{ph}} \frac{-\frac{K_e\omega}{V_{ph}} + \sqrt{1 + \left(\xi \frac{K_e\omega}{V_{ph}}\right)^2 - \xi^2 \left(\frac{K_e\omega}{V_{ph}}\right)^4}}{\left(\xi \frac{K_e\omega}{V_{ph}}\right)^2 + 1} \tag{5}$$

where $\xi=(N_p L_{ph} V_{ph})/(R_{ph} K_e)$.

2.3 TN Curves with Three Operation Zones

The TN curve of the motor can be specified by three operation zones: zone I, constant torque; zone II, maximum direct current (DC); and zone III, maximum voltage, shown as the thin solid curve a-p-q-C in Fig. 3. All of the operation points on any one of the TN curves must satisfy the equations presented below through the assumptions that (1) the motor inductance is neglected, (2) the power conversion between the DC and three-phase terminals is conserved, and (3) the three-phase voltages are constructed using space-vector pulse-width modulation (SVPWM) [3].

(A) Phase voltage and DC voltage modulation equation

$$V_{ph} = \frac{1}{\sqrt{3}} M_i V_{DC} \tag{6}$$

where V_{ph} is the peak of sinusoidal phase voltage of the motor; V_{DC} is the voltage of the DC source; and M_i is a modulation index which is positive but less than 1[4].

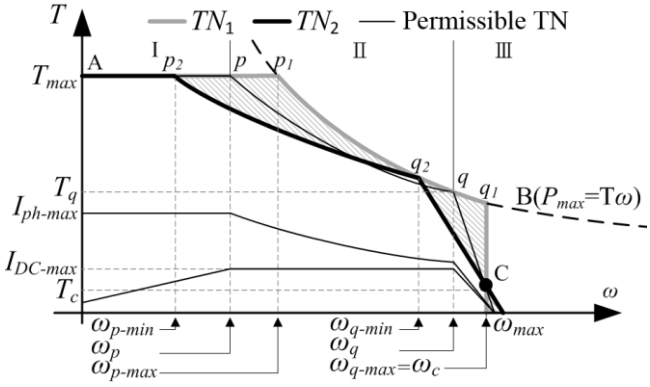

Figure 3: Target TN curve, its corresponding DC and phase currents, and two boundaries of the TN curves

(B) Phase current and DC current modulation equation

$$I_{DC} = \frac{\sqrt{3}}{2} M_i I_{ph} \tag{7}$$

where I_{DC} is the current of the DC source.

(C) Motor torque equation

$$T = \frac{3}{2} K_e I_{ph} \tag{8}$$

where T is the torque production of a three-phase motor driven by sinusoidal currents, each with a phase angle of 120°E.

(D) Steady-state electrical equation

When the phase current is fed in phase with the back EMF wave, voltage equations (3) and (4) with i_d=0 become

$$V_{ph} = R_{ph} I_{ph} + K_e \omega \tag{9}$$

During the constant torque, zone I, the maximum torque T_{max} is produced at the maximum phase current $I_{ph\text{-}max}$, and the phase voltage V_{ph} is controlled by a modulation index M_i so that $T_{max}=(3/2)K_e I_{ph\text{-}max}$ over the speed range of [0, ω_p]. It is assumed that no power is lost during the power conversion, and the current drawn from the DC terminal increases linearly with respect to the motor speed, according to (7), where M_i is adjusted from M_{min} to M_1. The minimum modulation index M_{min} occurs when ω=0, and it is calculated by (6) and (9); whereas, M_1 is calculated by (7) and (8) when the maximum DC current $I_{DC\text{-}max}$ is drawn from the power source at $\omega=\omega_p$. The maximum motor speed ω_p of zone I is then calculated using (6) through (9), and is expressed as

$$\omega_p = \left[\frac{\sqrt{M_1^{\,2} + (\xi M_{\min})^2 \left(M_1^{\,2} - M_{\min}^{\,2}\right)} - M_{\min}}{1 + (\xi M_{\min})^2} \right] \omega_{\max} \tag{10}$$

Beyond $M_i=M_1$, the motor operates at the maximum DC current $I_{DC\text{-}max}$ in zone II, and the phase voltage and current are adjusted from M_1 until it increases to its maximum value 1. The relationship between torque and speed is governed by a hyperbola of (5), as shown in Fig. 3. The maximum motor speed ω_q of zone II is then calculated using (6) through (9), and is expressed as

$$\omega_q = \left[\frac{\sqrt{1 + (\xi M_1 M_{\min})^2 \left(1 - M_1^{\,2} M_{\min}^{\,2}\right)} - M_1 M_{\min}}{1 + (\xi M_1 M_{\min})^2} \right] \omega_{\max} \tag{11}$$

In zone III, the motor operates at the maximum phase voltage $V_{ph}=V_{DC}/\sqrt{3}$. The relationship between torque and the speed higher than ω_q is approximated by a straight line, which is derived by (5) for ξ=0 as

the inductance is neglected. This line also passes the maximum motor speed point C, as shown in Fig. 3, and is expressed as

$$T = -\frac{3}{2}\frac{K_e^2}{R_{ph}}(\omega - \omega_c) + T_c \tag{12}$$

where T_c is the torque required for the motor at the maximum speed ω_c on a slope of 5%.

2.4 Boundaries of the TN Curves

In (5), the motor torque is a function of phase resistance, phase inductance, and the back EMF constant, and there might be infinite sets of TN curves that satisfy the driving scenario and the motor and drive properties. The boundaries of the TN curves are determined by assuming extreme conditions. When the phase inductance L_{ph} is negligibly small, the TN curve can be approximated by a straight line between ($3K_eV_{ph}/2R_{ph}$, 0) and (0, V_{ph}/K_e) for ξ=0. In the extreme case of $R_{ph}=\varepsilon$ ($0<\varepsilon<<1$), the straight line becomes perpendicular to the speed axis, so that the maximum value of corner speed $\omega_{q\text{-}max}$ is equal to ω_c. The corresponding back EMF constant of this vertical line has a maximum value

$$K_{e-\max} = \frac{V_{DC}}{\sqrt{3}\omega_C}. \tag{13}$$

This vertical boundary connects the hyperbola $P_{max}=T\omega$ at q_1 and intersects the maximum torque line at p_1 in zone I. Here, we complete the first boundary curve TN_1 which links A-p_1-q_1-C.

The other boundary of the TN curves is determined under the constraint of the maximum DC current $I_{DC\text{-}max}$ supplied by the battery in zone II and zone III. By assuming L_{ph}=0 for zone III, where M_i=1, the maximum phase resistance allowed for the motor to operate at its maximum power $P_{max}=T\omega$ is obtained by

$$R_{ph\text{-}max} = \frac{V_{dc}I_{DC\text{-}max} - P_{max}}{2I_{DC\text{-}max}^2}. \tag{14}$$

From (9), the maximum motor speed ω_{max} in zone III is expressed as $V_{DC}/\sqrt{3}\,K_e$ as I_{DC} and T approach 0. Substituting these values into (12) gives the relationship between R_{ph} and K_e as

$$3\omega_c K_e^2 - \sqrt{3}V_{DC}K_e + 2T_cR_{ph} = 0. \tag{15}$$

The minimum $K_{e\text{-}min}$ is obtained by substituting $R_{ph\text{-}max}$ into (15), and this determines the slope of line (12) in zone III. This straight line intersects with curve B at q_2, and the hyperbola (5) with the same $K_{e\text{-}min}$ and $R_{ph\text{-}max}$ in zone II connects the constant torque curve in zone I at p_2. Here, we complete the second boundary curve TN_2, which links A-p_2-q_2-C.

All the TN curves in the ranges of $K_{e\text{-}min}<K_e<K_{e\text{-}max}$ and $R_{ph\text{-}min}<R_{ph}<R_{ph\text{-}max}$ satisfy the three driving scenarios. By using the driving parameters and constraints given in Table 1, the boundary TN curves and their corresponding motor and drive parameters are calculated and illustrated in Table 2.

Table 2: Motor and drive parameters for the TN boundaries

Boundary	TN_1		TN_2	
K_e (V/rad/s)	$K_{e\text{-}max}$	0.512	$K_{e\text{-}min}$	0.441
R_{ph} (Ω)	$R_{ph\text{-}min}$	ε ($0<\varepsilon\ll1$)	$R_{ph\text{-}max}$	0.641
ω_{max} (rpm)	4094 (=ω_c)		4884	
$I_{DC\text{-}max}$ (A)	70.4		81.8	
$I_{ph\text{-}max}$ (A)	173.5		201.4	
ω_p (rpm)	$\omega_{p\text{-}max}$	1918	$\omega_{p\text{-}min}$	631
ω_q (rpm)	$\omega_{q\text{-}max}$	4094	$\omega_{q\text{-}min}$	3225
T_q (Nm)	T_{q1}	47.58	T_{q2}	60.40

3 Quasi-3D Magnetic Circuit Model

All of the design parameters of the AFPM motor shown in Fig. 4(a) for the EV are presented in Table 3. It is approximately to slice the AFPM motor into rings of different radii, and each ring is extended as a 2-dimensional (2D) linear machine, as shown in Fig. 4(b) [5]. Fig. 4(c) shows a cross-section of each ring of the AFPM motor along a circumference of a radius ranging between R_o and R_i. The circumferential coordinate is denoted by x.

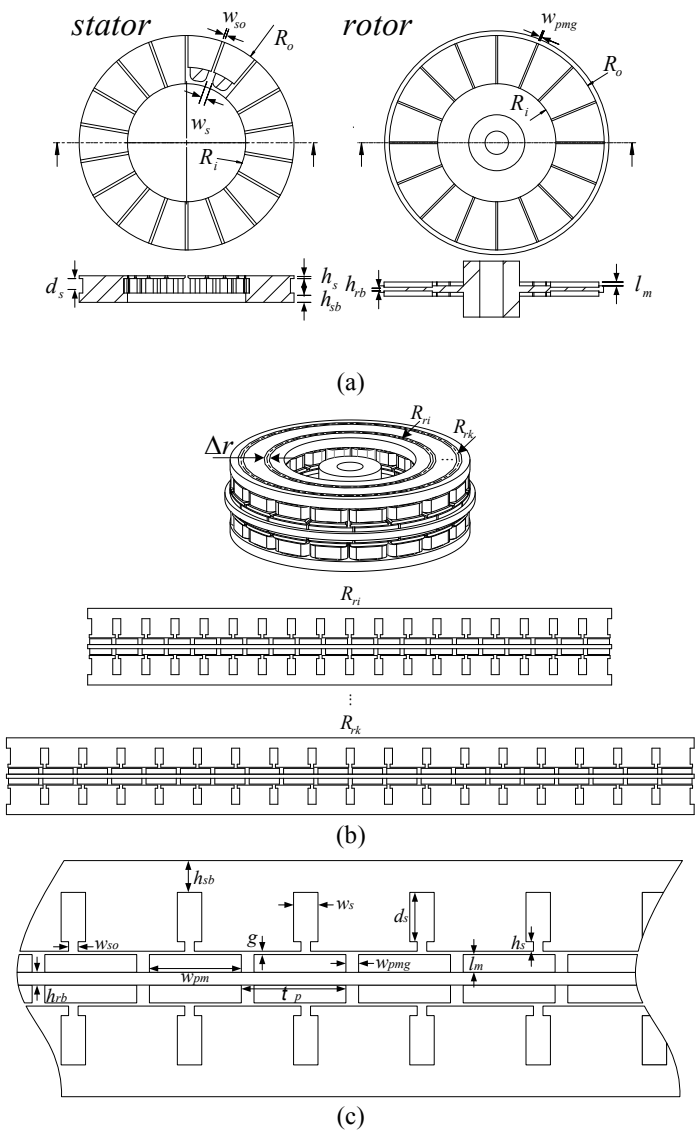

Figure 4: (a) Geometry of stator and rotor, (b) geometry of quasi-3D magnetic circuit model, and (c) 2D cross-sectional view

Table 3: Design parameters

Inner radius	R_i	Slot width	w_s
Outer radius	R_o	Slot height	d_s
Stator back iron thickness	h_{sb}	Shoe height	h_s
Rotor back iron thickness	h_{rb}	Slot opening	w_{so}
Air-gap length	g	Magnet length	l_m
Number of slots	N_s	Magnet gap	w_{pmg}
Number of poles	N_m	No. of turns	N

It is assumed that there is no fringing effect and no magnetic flux in the radial direction, so that each of the linear machines is independent. The overall performance of an AFPM motor will be the sum of the performance of all of the linear machines when a linear magnetic property is assumed in the following magnetic circuit analysis. The air-gap flux density distribution for slotless configuration is adopted from [6]

$$B_{pm}(x)=\sum_{n=1,3,5,\ldots}^{\infty}\frac{-\frac{8B_r}{n\pi}\sin\left(\frac{\alpha_p n\pi}{2}\right)\exp\left(\frac{n\pi g}{\tau_p}\right)\left(\exp\left(\frac{n\pi l_m}{\tau_p}\right)-1\right)\cos\left(\frac{n\pi}{\tau_p}x\right)}{(1+\mu_R)\left(1-\exp\left(\frac{2n\pi(g+l_m)}{\tau_p}\right)\right)+(1-\mu_R)\left(\exp\left(\frac{2n\pi g}{\tau_p}\right)-\exp\left(\frac{2n\pi l_m}{\tau_p}\right)\right)} \tag{16}$$

where B_r is the remanence flux density and α_p is the ratio between the magnet width w_{pm} and the pole pitch τ_p. As the rotor rotates, the relative position of the rotor and stator, which is defined as the rotor shift s, varies, and the air-gap flux density is not only a function of peripheral coordinate x but also a function of rotor shift s. By considering the stator slotting effect, the air-gap flux density must be reduced by additional air-gap reluctance. The air-gap flux density distribution function is then modified as

$$B_g(x,s)=\Pi(x)B_{pm}(x-s) \tag{17}$$

where $\Pi(x)$ is the relative permeance, which is defined as the ratio between the equivalent air gap with and without slots, as follows

$$\Pi(x)=\frac{\frac{l_m}{\mu_R}+g}{\frac{l_m}{\mu_R}+g_e(x)} \tag{18}$$

where g_e is the effective air-gap length and μ_R is the recoil permeability of the magnet [7].

This air-gap flux density distribution is compared with the result obtained from the 2D FE method for an example of s=0°E, as shown in Fig. 5(a). In the FE analysis, the flux density becomes high near the fringe of the slot (location a) because of the flux saturation that was not modeled on the vertex of the stator teeth in the magnetic circuit model. A modeling error near the center of the slot (location b) also causes modeling errors in the preliminary motor design. The corresponding flux linkage of phase A is calculated, and it matches very well with the value obtained using the 2D FE method, as shown in Fig. 5(b).

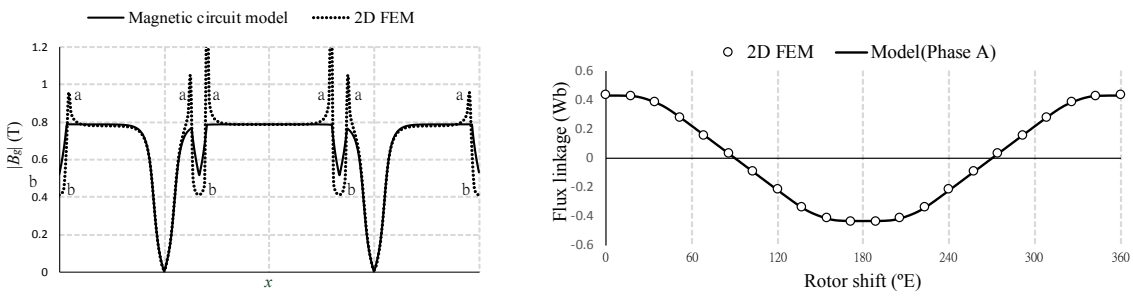

(a) (b)

Figure 5: (a) Comparison of the air-gap flux density distributions between the analytical and 2D FE methods (s=0°E), (b) comparison of the flux linkage of phase A between the analytical and 2D FE methods

4 Motor Sizing and Optimization

4.1 Motor Sizing

According to the AFPM motor parameters presented in Table 2, the motors with slot and pole combinations of 12/14, 18/16, and 18/20, which are simply referred to the 12/14 motor, the 18/16 motor, and the 18/20 motor, have satisfactory winding factors of 0.933, 0.945, and 0.945, respectively, and they are promising candidates for the following optimal design. As shown in Table 3, 14 design parameters need to be determined. It is necessary to begin the sizing by assigning reasonable values to the independent design parameters, such as the air-gap length g, the magnet gap w_{pmg}, and the shoe height h_s. Most of the other parameters are dependent variables, and they are determined by the motor geometry and performance equations so that the design targets of K_e and R_{ph} are satisfied. Through the process of calculating the size of the motor, three sets of motors, a 12/14 motor, an 18/16 motor, and an 18/20 motor, were obtained by changing different active parameters—the magnet length l_m, the outer radius R_o, and the inner radius R_i, within a reasonable range.

4.2 Multi-objective Optimization

The AFPM motor is designed to minimize energy consumption based on the motor weight and the frequent operating points of a driving cycle. The best motor size set is then determined using the following three design objectives or performance indices.

4.2.1 Motor weight

The first design objective is to minimize the active motor weight that consists of the stator weight W_s, the rotor weight W_r, and the winding weight W_w, which are all explicitly written in terms of the motor parameters shown in Table 3

$$\text{Min.} \quad W = W_s + W_r + W_w \tag{19}$$

4.2.2 Energy loss during the driving cycles

The second motor design objective is for the EV to achieve a high driving efficiency over various driving cycles. The three driving cycles that are widely used, FTP-75, NEDC, and JC08, are shown in Fig. 6(a). The corresponding equally sampled operation points plotted on the TN map are shown in Fig. 6(b). Although the driving efficiency depends on various subsystems, such as the battery bank, the power inverter, the motor, the drive train gears, and the differentials, minimizing total energy loss of the motor is our major concern, and is formulated as follows

$$\text{Min.} \quad EL = \sum_{i=1}^{n}\left[k_F P_{l,F}(\omega_i, T_i) + k_N P_{l,N}(\omega_i, T_i) + k_J P_{l,J}(\omega_i, T_i)\right]\Delta t \tag{20}$$

where EL is the total energy loss of the motor during the driving cycle; $P_{l,F}$, $P_{l,N}$, and $P_{l,J}$ are the power losses of the motor at the operation points of driving cycles FTP-75, NEDC, and JC08, respectively; and Δt is the operation time interval. Different weighing factors, k_F, k_N, and k_J, are also assigned to these driving cycles.

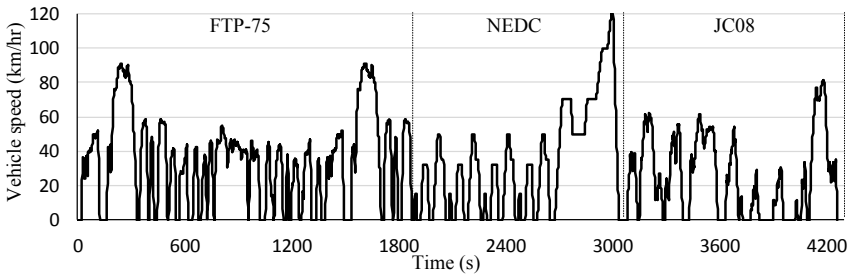

(a)

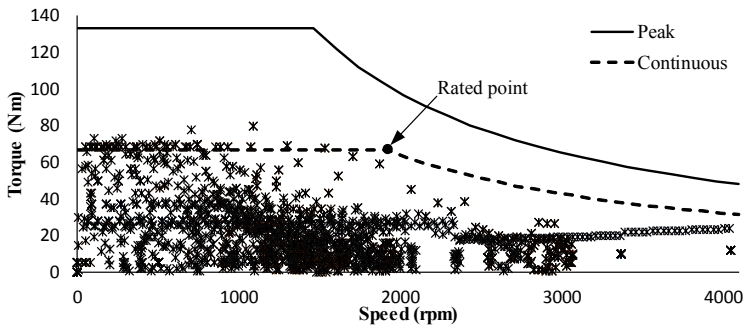

(b)

Figure 6: (a) The target driving cycles and (b) distribution of the corresponding operating points

4.2.3 Efficiency at the rated operation point

In order to compare the results of the proposed motor design with the traditional design method, only the efficiency of the rated operation point was maximized. The third design objective is written as the rated efficiency of the motor at the corner point, in Fig. 6(b), on the continuous TN curve

$$\text{Max. } \eta_r = \frac{T_r \omega_r}{T_r \omega_r + P_r + P_c + P_s} \tag{21}$$

where ω_r is the rated speed, T_r is the rated torque, P_r is the core loss, P_c is the copper loss, and P_s is the stray loss. Here, the rated torque T_r is an implicit function of the design variables, and it is calculated using (5) via analytical magnetic circuit models.

The compromise programming method in the multifunctional optimization system tool (MOST) [8] was applied to search for the optimal values of the design variables that maximize or minimize the above performance indices (19)-(21). During the optimization, different weighing factors were assigned to describe the different levels of importance of the three objectives. Table 4 illustrates the best five results from the multi-objective optimization process. While the 18/20 motor was identified as the best result in four out of five cases, the 18/16 motor is inferior to the other motors and it was abandoned.

As expected, the 18/20 motor has a shorter end winding and a thinner back iron than the other two candidates, but it has a large radius because it has a large number of poles. Among the 18/20 candidate motors, Case 2 provides a motor with a minimum weight, but the worst rated efficiency; Case 3 has the least energy loss or the best driving-cycle efficiency, but the heaviest weight; and Case 5 has the highest rated efficiency, but the highest energy loss. Case 4 and Case 5 were found to have a more than 15% additional energy loss than the motor designed by traditional approaches without considering the frequent operation points. Therefore, Case 1, in which both the motor weight and the energy loss during the driving cycles are minimized, is the best choice for further verification and refinement using FE analysis.

Table 4: Multi-objective optimization results

Case			1	2	3	4	5
Weighing factor	Motor weight (W)		0.7	0.85	0	0.8	0
	Energy loss (EL)	FTP-75	0.1	0.05	1/3	0	0
		NEDC	0.1	0.05	1/3	0	0
		JC08	0.1	0.05	1/3	0	0
	Rated efficiency (η_r)		0	0	0	0.2	1
	N_s		18	18	12	18	18
	N_m		20	20	14	20	20
	R_o (mm)		108	105	103	106	116
	R_i (mm)		56	66	47	55	56
	l_m (mm)		4.5	6.9	5.8	6.6	6.8
	Weight (kg)		11.60	10.92	13.92	11.82	13.82
	Energy loss (kJ)		796.72	818.98	763.08	808.02	898.83
	Efficiency (%)		93.28	93.14	93.19	93.40	93.45
	K_e (V/rad/s)		0.485	0.485	0.485	0.490	0.504
	L_{ph} (μH)		208.71	207.44	288.33	176.79	127.57
	R_{ph} (ohm)		0.0438	0.0444	0.0471	0.0430	0.0406
Zone I	T_{max} (Nm)		133.34	133.23	133.20	134.63	138.59
	ω_p *(rpm)*		1491	1503	1547	1555	1620
Zone II	P_{max} (kW)		26.10	26.11	26.17	26.57	27.21
	Rated torque @ 4094 rpm		32.18	32.18	32.19	32.34	32.54
Zone III	ω_{max} (rpm)		4320	4323	4324	4278	4156

5 Finite Element Analysis

The above optimization results were obtained from the quasi-3D magnetic circuit model, which is usually relatively imprecise because of the assumption of linear properties and the simplified motor configuration. The exploded view of the proposed AFPM motor is illustrated in Fig. 7(a), where the motor housing on each side of the stator is responsible for dissipating heat loss via the water-cooling duct. It is necessary to apply FE analysis to verify the optimal design results. The magnetic flux density distributions in the rotor, stator, and air gap at the peak phase current of 200 A are illustrated in Fig. 7(b). The maximum flux density of 1.8 T occurs at some locations on the stator teeth and the back iron as well as in the air gap along the outer radius near 95 mm. Thus, the motor performances were analyzed in terms of the back EMF wave, the TN curve, the efficiency map, the energy loss over various driving cycles, and the heat dissipation properties.

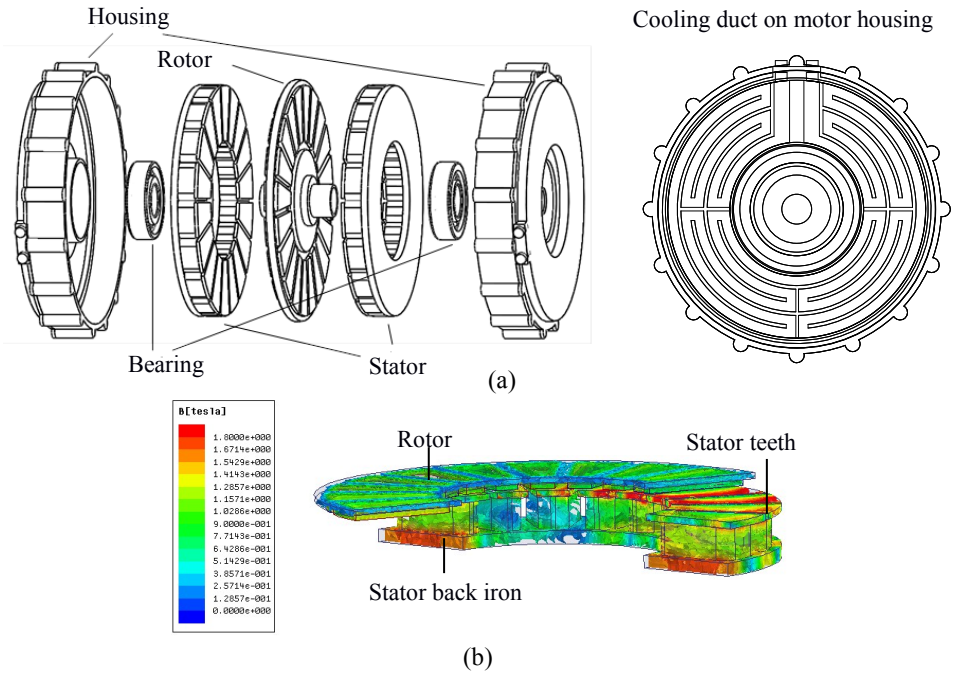

Figure 7: (a) Exploded view of the AFPM motor assembly and water-cooling duct on housing, magnetic flux density distribution in (b) the stator and the rotor

5.1 TN Curve and Efficiency Map

The resulting TN curve was obtained and compared with the TN curve required by the three driving scenarios and the TN curve obtained using the magnetic circuit model, as shown in Fig. 8. It was found that the operation range of the proposed motor was wider than the TN curve that was obtained using the magnetic circuit model in zone III. As shown in Table 5, the maximum motor speed 4428 rpm increased by 2.5% because the final back EMF constant was found to be smaller than the back EMF constant obtained using the magnetic circuit model. The difference in operation zone II is due to the fact that the phase inductance obtained using FE analysis is higher than the phase inductance obtained using the magnetic circuit model. Due to the coupling effect of phase inductance and resistance, the first corner speed from the FE analysis was found to be slightly lower than the required corner speed.

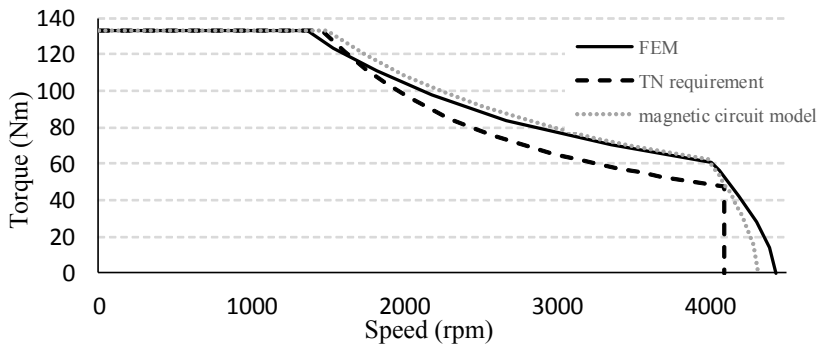

Figure 8: The resulting TN curve using the FE method as compared to the required TN curve and the TN curve obtained using the magnetic circuit model

Table 5. Comparison of TN curve parameters

Model	$I_{ph\text{-}max}$ (A)	ω_p (rpm)	ω_q (rpm)	ω_{max} (rpm)	K_e (V/rad/s)	L_{ph} (μH)
Magnetic circuit	183.3	1491	4023	4320	0.485	208.71
Finite element	195.5	1363	4010	4428	0.473	237.18
error	+6.7%	-8.6%	-0.3%	+2.5%	-2.5%	+13.6%

Fig. 9 shows the efficiency map obtained from the FE method. At the rated point, the motor efficiency (93.40%) was found to be slightly higher than the motor efficiency (93.28%) obtained from the magnetic circuit model, as seen in the optimal Case 1 shown in Table 4.

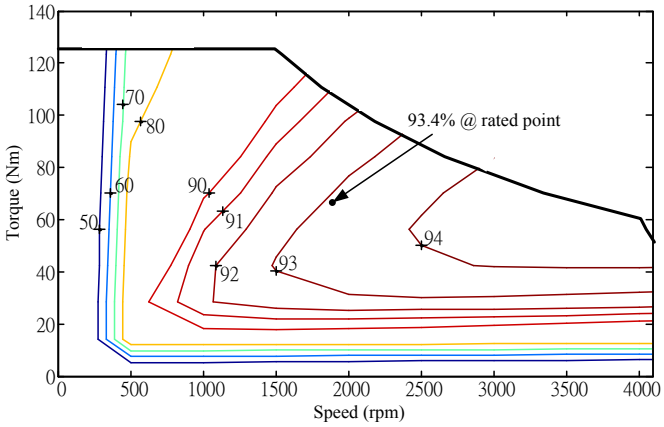

Figure 9: Efficiency map from the FE method

5.2 Energy Loss Analysis

Table 6 shows a comparison of the energy losses from the proposed AFPM motor when four of the motors drive the four-wheel-drive passenger car with three driving cycles (FTP-75, NEDC, and JC08). As seen in Table 6, the FE analysis results in higher copper loss, but lower iron loss, than the magnetic circuit model. This is because the permeability of electrical steel was assumed to be much larger than the permeability of air, so the reluctance of steel was neglected in the magnetic circuit model. Thus, the magnetic flux density distribution in the air gap, the back EMF constant, and the torque are all larger than those obtained using FE analysis. Therefore, more current is required in the FE model to produce the same torque as found in the magnetic circuit model. The eddy-current loss in the magnet is relatively small, and it is about 3% of the total loss. In general, there is only about a 5–7% difference in energy loss between the FE and magnetic circuit models.

Table 6: Comparison of energy loss with different driving cycles
(FEM: finite element model; MCM: magnetic circuit model)

Energy Loss (kJ/cycle)		Copper loss	Iron loss	Magnet loss	Total
FTP-75	FEM	106.98	255.52	11.19	373.69
	MCM	100.45	294.00	-	394.45
NEDC	FEM	32.50	184.44	8.66	225.60
	MCM	30.63	212.14	-	242.77
JC08	FEM	42.15	103.91	4.10	150.16
	MCM	39.66	119.84	-	159.50

6 Conclusions

This paper proposed a systematic, driving-scenario oriented, multi-objective optimal design process of an AFPM motor for a four-wheel-drive EV. The driving scenario, the modulation method of the motor drive, and basic torque and voltage equations of the motor were used to provide basic information for building a range of target TN curves for three operation zones—constant torque, maximum DC current, and maximum voltage. Thus, the back EMF constant, phase inductance, and phase resistance were used to size and optimize the proposed motor using a quasi-3D magnetic circuit model. The systematic optimal design process for a preliminary motor design was fast and accurate, as verified through FE analysis. First, the resulting TN curve was found to match well with the target TN curve. The corresponding efficiency maps of the FE and magnetic circuit methods were also found to be similar, with a difference of less than 3%. Second, the energy consumption of the proposed motor was 15% less than the energy consumption of the motor designed using a traditional method, which optimized the motor efficiency only at its rated operation point. Finally, the water-cooling duct was designed so that the motor dissipated energy loss during the operation. Moreover, the temperature response and steady-state temperature distributions were investigated, and it was proven that the proposed motor can be operated safely for a continuous driving mode.

Acknowledgments

The authors acknowledge the financial support of the National Science Council of Taiwan, Republic of China under Contract NSC 103-2221-E-002 -001. They are also grateful for the partial support by the Mechanical and Systems Research Laboratories of Industrial Technology Research Institute in Taiwan.

References

[1] S. Kahourzade1, A. Mahmoudi, N. A. Rahim and H. W. Ping. "Sizing equation and finite element analysis optimum design of axial-flux permanent magnet motor for electric vehicle direct drive," in IEEE International Power Engineering and Optimization Conference (PEDCO), Melaka, Malaysia, 2012.

[2] P. Lindh, J. Montonen, P. Immonen, J. A. Tapia and J. Pyrhonen. " Design of a traction motor with tooth-coil windings and embedded magnets," IEEE Transactions on Industrial Electronics, vol. 61, no. 8, pp. 4306-4314, Aug. 2014.

[3] Y. P. Yang and F. X. Ding, “Driving-scenario oriented design of an axial-flux permanent-magnet synchronous motor for a pedal electric cycle,” IET Electric Power Applications, vol. 9, Iss. 6, July 2015, pp. 420 – 428.

[4] N. Mohan, T. M. Undeland, and W. P. Robbins, Power Electronics: Converters, Applications, and Design, 3ed, John Wiley & Sons, 2002.

[5] A. Parviainen, M. Niemela, and J. Pyrhonen, "Modeling of Axial Flux Permanent-Magnet Machines," IEEE Transactions on Industry Applications, vol. 40, no. 5, pp. 1333-1340, Sep./Oct. 2004

[6] M. J. Chung and D. G. Gweon, "Modeling of the armature slotting effect in the magnetic field distribution of a linear permanent magnet motor, " in Arch. Elektrotech., 2002, vol. 84, pp. 101–108.

[7] D. Hanselman, Brushless permanent magnet motor design, McGraw-Hill, New York, 2nd ed., 2003.

[8] Y. P. Yang, Y. P. Luh, and C. H. Cheung, "Design and Control of Axial-Flux Brushless DC Wheel Motors for Electric Vehicles-Part I: Multiobjective Optimal Design and Analysis," IEEE Transactions on Magnetics, vol. 40, no. 4, pp. 1873-1882, Jul. 2004.

Authors

Guan-Yu Shih received the B.S. in mechanical engineering from National Cheng-Kung University, Taiwan, in 2012, and the M.S. degree in mechanical engineering from National Taiwan University, Taiwan, in 2015. He is currently working as an application engineer for the electromagnetic and multi-physics application at Taiwan Auto-Design Co., ANSYS channel partner in Taiwan.

Yee-Pien Yang received a B.S. and M.S. in mechanical engineering from National Cheng-Kung University in Taiwan, in 1979 and 1981, respectively, and a Ph.D. in Mechanical, Aerospace, and Nuclear Engineering from the University of California, Los Angeles in 1988. He is now a professor in the Department of Mechanical Engineering of National Taiwan University, leading the propulsion control laboratory and conducting research on the design and control of electromechanical systems, and assistive tool design for the disabled. He is also a researcher at the Industrial Technology Research (ITRI), Taiwan.